

## Article

# Simultaneous Observation of Tungsten Spectra of $W^0$ to $W^{46+}$ Ions in Visible, VUV and EUV Wavelength Ranges in the Large Helical Device

Tetsutarou Oishi <sup>1,2,\*</sup> , Shigeru Morita <sup>1,2</sup> , Daiji Kato <sup>1,3</sup> , Izumi Murakami <sup>1,2</sup> , Hiroyuki A. Sakaue <sup>1</sup>, Yasuko Kawamoto <sup>1</sup> , Tomoko Kawate <sup>1,2,4</sup>  and Motoshi Goto <sup>1,2</sup> 

- <sup>1</sup> National Institute for Fusion Science, National Institutes of Natural Sciences, 322-6 Oroshi-cho, Toki, Gifu 509-5292, Japan; morita@nifs.ac.jp (S.M.); dkato@nifs.ac.jp (D.K.); mizumi@nifs.ac.jp (I.M.); sakaue@nifs.ac.jp (H.A.S.); kawamoto.yasuko@nifs.ac.jp (Y.K.); kawate.tomoko@nifs.ac.jp (T.K.); goto@nifs.ac.jp (M.G.)
- <sup>2</sup> Department of Fusion Science, The Graduate University for Advanced Studies, SOKENDAI, 322-6 Oroshi-cho, Toki, Gifu 509-5292, Japan
- <sup>3</sup> Interdisciplinary Graduate School of Engineering Sciences, Kyushu University, Kasuga, Fukuoka 816-8580, Japan
- <sup>4</sup> National Astronomical Observatory of Japan, 2-21-1 Osawa, Mitaka, Tokyo 181-8588, Japan
- \* Correspondence: oishi@nifs.ac.jp

**Abstract:** Spectroscopic studies for emissions released from tungsten ions have been conducted in the Large Helical Device (LHD) for contribution to the tungsten transport study in tungsten divertor fusion devices and for expansion of the experimental database of tungsten line emissions. Tungsten ions are distributed in the LHD plasma by injecting a pellet consisting of a small piece of tungsten metal wire enclosed by a carbon tube. Line emissions from  $W^0$ ,  $W^{5+}$ ,  $W^{6+}$ ,  $W^{24+}$ – $W^{28+}$ ,  $W^{37+}$ ,  $W^{38+}$ , and  $W^{41+}$ – $W^{46+}$  are observed simultaneously in the visible (3200–3550 Å), vacuum ultraviolet (250–1050 Å), and extreme ultraviolet (5–300 Å) wavelength ranges and the wavelengths are summarized. Temporal evolutions of line emissions from these charge states are compared for comprehensive understanding of tungsten impurity behavior in a single discharge. The charge distribution of tungsten ions strongly depends on the electron temperature. Measurements of emissions from  $W^{10+}$  to  $W^{20+}$  are still insufficient, which is addressed as a future task.

**Keywords:** plasma spectroscopy; visible light; vacuum ultraviolet; extreme ultraviolet; magnetically confined fusion; impurity transport; highly ionized tungsten ions



**Citation:** Oishi, T.; Morita, S.; Kato, D.; Murakami, I.; Sakaue, H.A.; Kawamoto, Y.; Kawate, T.; Goto, M. Simultaneous Observation of Tungsten Spectra of  $W^0$  to  $W^{46+}$  Ions in Visible, VUV and EUV Wavelength Ranges in the Large Helical Device. *Atoms* **2021**, *9*, 69. <https://doi.org/10.3390/atoms9030069>

Academic Editor: Jean-Christophe Pain

Received: 1 September 2021

Accepted: 15 September 2021

Published: 17 September 2021

**Publisher's Note:** MDPI stays neutral with regard to jurisdictional claims in published maps and institutional affiliations.



**Copyright:** © 2021 by the authors. Licensee MDPI, Basel, Switzerland. This article is an open access article distributed under the terms and conditions of the Creative Commons Attribution (CC BY) license (<https://creativecommons.org/licenses/by/4.0/>).

## 1. Introduction

Tungsten (W) is considered as a candidate material for plasma-facing components (PFCs) in the divertor region of the international thermonuclear experimental reactor (ITER) and future fusion reactors because of its high melting point, low sputtering yield, and low tritium retention [1–3]. On the other hand, there is a concern that tungsten ions with a large atomic number of  $Z = 74$  will cause large energy loss by radiation and ionization when the plasma is contaminated by the W impurity. Therefore, it is very important to investigate the behavior of tungsten in high temperature plasmas in order to control tungsten transport and establish reliable operation scenarios for fusion reactors. Since tungsten is high- $Z$  and can take a wide range of charge states, the wavelength range to be covered by spectroscopy is also wide. Therefore, efforts to compile a database of the emission spectra of tungsten ions with a wide range of charge states are actively conducted [4], and spectroscopic diagnostics to further accumulate spectral data have been continuously carried out in basic experiments such as the electron beam ion trap (EBIT) and magnetic field confinement plasma experiments [5–10].

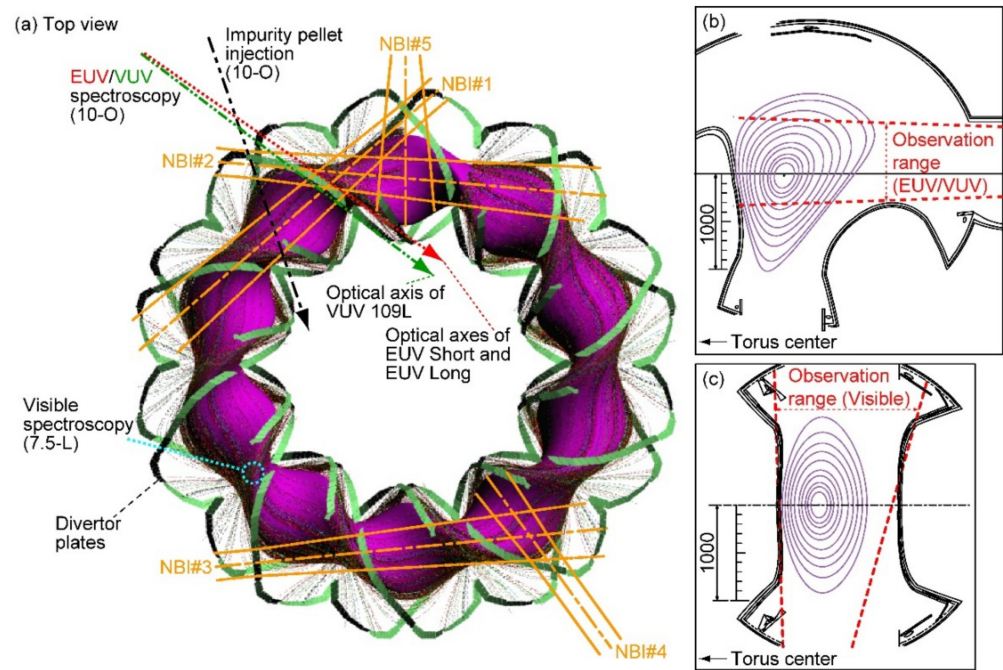
Spectroscopic studies for emission from W ions in combination with a tungsten pellet injection technique have been intensively conducted on the Large Helical Device (LHD) for

contribution to tungsten transport studies in tungsten divertor fusion devices represented by ITER and for expansion of the experimental database of tungsten line emissions [11–14]. The electron temperature,  $T_e$ , of the LHD core plasmas with a tungsten pellet injection ranges from 0.5 keV to 3.5 keV, which is close to that of the edge plasmas in ITER around the last closed flux surface, including the scrape-off layer. Thus, observation of tungsten lines in LHD could improve the tungsten diagnostics in ITER edge plasmas. The current status of tungsten emission lines observed in LHD using visible, vacuum ultraviolet (VUV), and extreme ultraviolet (EUV) spectroscopy can be summarized as follows. The line emissions from the neutral atoms,  $W^0$ , as well as the singly ionized ions,  $W^+$ , were observed using visible spectroscopy in the wavelength range of 4000–4400 Å [11]. The visible spectroscopy has also observed magnetic dipole (M1) forbidden transition lines from  $W^{26+}$  and  $W^{27+}$  in the wavelength range of 3300–3900 Å [15–17]. The line emissions from tungsten ions in low charge states,  $W^{2+}$ – $W^{6+}$ , have been identified in the VUV range of 500–1500 Å [18]. Recently, several M1 lines of  $W^{29+}$ – $W^{39+}$  were successfully observed in the VUV wavelength range of 500–900 Å [19]. Additionally, in the EUV range of 5–500 Å, tungsten ions in low charge states,  $W^{4+}$ – $W^{7+}$ , medium charge states,  $W^{24+}$ – $W^{33+}$  in the structures of the unresolved transition array (UTA), as well as high charge states,  $W^{41+}$ – $W^{46+}$ , have been identified [20–22]. This paper is dedicated to summarizing the tungsten spectra in the visible, VUV, and EUV wavelength ranges based on the progress of line identifications. Temporal evolution of emissions from tungsten ions in various charge states that are observed simultaneously will also be demonstrated for comprehensive understanding of behavior of tungsten impurity.

## 2. Tungsten Pellet Injection Experiment in LHD

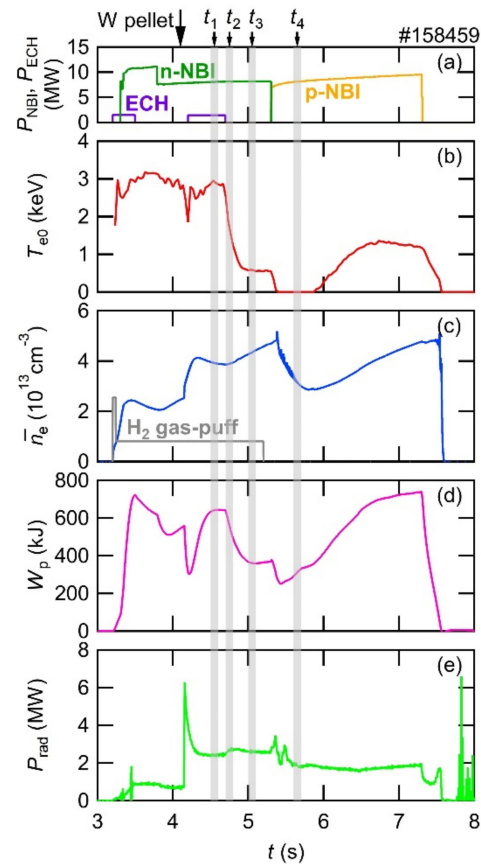
LHD is a heliotron-type plasma confinement device which has the major/minor radii of 3.6/0.64 m in the standard configuration with a maximum plasma volume of 30 m<sup>3</sup> and toroidal magnetic field of 3 T [23]. The coil system consists of a set of two continuous superconducting helical coils with a poloidal pitch number of two and a toroidal pitch number of 10 and three pairs of superconducting poloidal coils. Figure 1a illustrates the top view of the shape of the plasma in the LHD device together with schematic drawings of the neutral beam injection (NBI) for heating, the impurity pellet injection, and the spectroscopic diagnostics consisting of two flat-field grazing incidence EUV spectrometers (denoted as “EUV Short” [24] and “EUV Long” [25]), a normal incidence 20 cm VUV spectrometer (denoted as “VUV 109L” [26]), and an astigmatism-corrected Czerny–Turner-type 30 cm visible spectrometer (denoted as “MK300” [27]). Neutral hydrogen atoms are used as beam particles in the experiments presented in this paper. NBIs #1, 2, and 3, which have negative ion sources (n-NBI), are injected tangentially to the magnetic axis, while #4 and 5 with positive ion sources (p-NBI) are injected perpendicular to the magnetic axis. Tungsten ions are distributed in the NBI-heated LHD plasma by injecting a pellet consisting of a small piece of tungsten metal wire enclosed by a carbon or polyethylene pellet with the shape of a cylindrical tube [13]. Figure 1b,c illustrate the cross sections of the magnetic surfaces, where the optical axes of the VUV/EUV and visible spectroscopy systems are located, respectively, together with the field of view of each system. The EUV Short, EUV Long, and VUV 109L spectrometers cover the wavelength ranges of 5–60 Å, 100–300 Å, and 250–1050 Å, respectively. CCD detectors (1024 × 256 pixels, pixel size 26 × 26 μm<sup>2</sup>, Andor DO420-BN) are placed at the positions of the exit slits of the spectrometers. A CCD data acquisition operational mode applied in this experiment is called “full-binning” mode, in which all CCD-pixels aligned in the vertical direction are replaced by a single channel, and the vertical spatial resolution is entirely eliminated. The time resolution for the spectra measurements is 5 ms in the full-binning data acquisition mode. The MK300 visible spectrometer covers the wavelength range of 3200–3550 Å. A CCD detector (1024 × 1024 pixels, pixel size 13 × 13 μm<sup>2</sup>, Andor DU934-N) is placed at the position of the exit slit of the spectrometer and is operated in the sub-image data acquisition mode with a sampling time of 100 ms, including an exposure time of 61.55 ms. Although this

spectrometer usually divides the field of view into 40 observation chords to measure the spatial distribution of the emission [28], in this paper we used the spectra obtained by integrating all 40 observation chords.



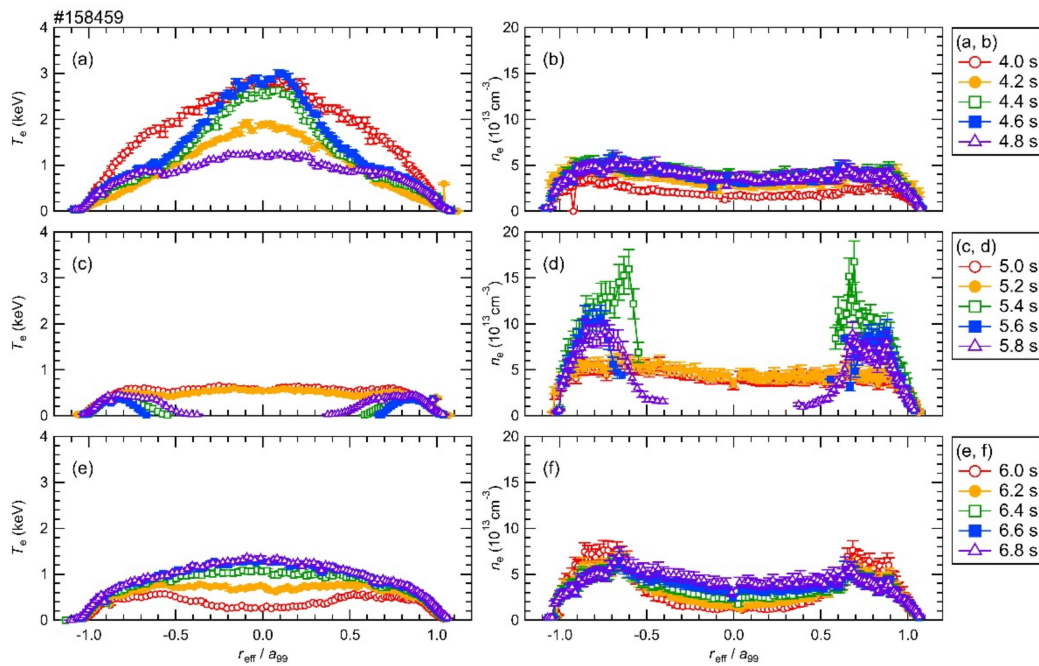
**Figure 1.** (a) Top view of shape of plasma in LHD device together with schematic drawings of neutral beam injection (NBI) for heating, spectroscopic diagnostics, and impurity pellet injection. Cross sections of magnetic surfaces where optical axes of (b) VUV/EUV and (c) visible spectroscopy systems are located, respectively, together with viewing angle of each system.

Figure 2 shows a typical waveform of the tungsten pellet injection experiment in a hydrogen discharge with the position of the magnetic axis,  $R_{ax}$ , at 3.6 m at a toroidal magnetic field,  $B_t$ , of 2.75 T in the counter-clockwise direction. In this discharge, the length and diameter of a tungsten wire enclosed in a carbon pellet were 0.7 mm and 0.1 mm, respectively. Then, the number of tungsten atoms enclosed in a pellet,  $N_W$ , was  $3.5 \times 10^{17}$ . As shown in Figure 2a, the plasma was initiated by electron cyclotron heating (ECH), and further heated by the neutral hydrogen beams. Figure 2b–e show the central electron temperature,  $T_{e0}$ , the line-averaged electron density,  $\bar{n}_e$ , the plasma stored energy,  $W_p$ , and the total radiation power,  $P_{rad}$ , respectively. In order to obtain  $T_{e0}$ , the electron temperature measured by Thomson scattering at the location of  $-0.1 < r_{eff}/a_{99} < 0.1$  was averaged, where  $r_{eff}$  is the effective minor radius and  $a_{99}$  is the plasma edge, defined as the effective minor radius in which 99% of electron stored energy was enclosed [29]. After the tungsten pellet injection at 4.1 s,  $T_{e0}$  and  $W_p$  quickly decreased, while  $n_e$  increased. ECH was superposed for 4.2–4.7 s; then,  $T_{e0}$  recovered up to around 3 keV. After the ECH was turned off,  $T_{e0}$  decreased and kept the value around 0.6 keV for 5.0–5.3 s. The NBI heating scheme was switched from the n-NBIs to p-NBIs at 5.3 s. Then,  $T_{e0}$  decreased down to a very low level close to zero for 5.4–5.9 s, followed by a recovery to a value of around 1.4 keV due to continuous heating by p-NBIs. In this paper, spectral data were obtained at four different timings with different  $T_{e0}$ , namely  $t_1 = 4.5$  s ( $T_{e0} \sim 3.0$  keV),  $t_2 = 4.7$  s ( $T_{e0} \sim 1.7$  keV),  $t_3 = 5.0$  s ( $T_{e0} \sim 0.6$  keV), and  $t_4 = 5.6$  s ( $T_{e0} \sim 0$  keV), as indicated in Figure 2, to demonstrate the effect of the electron temperature on the observable charge states of the tungsten ions.



**Figure 2.** Typical waveform of W pellet injection experiment in LHD: (a) heating power of ECH, n-NBI, and p-NBI, (b) central electron temperature, (c) line-averaged electron density, (d) plasma stored energy, and (e) total radiation power. Four timings of data acquisition,  $t_1 = 4.5$  s,  $t_2 = 4.7$  s,  $t_3 = 5.0$  s, and  $t_4 = 5.6$  s are indicated together.

Figure 3 shows temporal evolutions of radial profiles of the electron temperature,  $T_e$ , and the electron density,  $n_e$ , Figure 3a,b for 4.0–4.8 s, Figure 3c,d for 5.0–5.8 s, and Figure 3e,f for 6.0–6.8 s, plotted against  $r_{eff}/a_{99}$ . After the pellet injection at 4.1 s,  $T_e$  decreased over the entire region within the plasma edge, and then recovered in the central region of the plasma at about  $-0.6 < r_{eff}/a_{99} < 0.6$  due to the ECH superposition for 4.2–4.7 s, as shown in Figure 3a.  $n_e$  increased after the pellet injection, keeping a flat radial profile as shown in Figure 3b. When the NBI heating scheme was switched from the n-NBIs to p-NBIs at 5.3 s, both the  $T_e$  and  $n_e$  profiles became extremely hollow, as shown in Figure 3c,d. In this paper, the emission spectra with the central electron temperature close to zero are presented as “the spectrum with  $T_{e0} = 0$  keV”, but note that the actual emission is from the peripheral part of the plasma with a finite electron temperature, which surrounds the central part with a very low electron temperature. Thereafter, both of the central  $T_e$  and  $n_e$  recovered due to a continuous heating by p-NBIs, as shown in Figure 3e,f. The large variation of  $T_e$  after the pellet injection as shown in Figures 2 and 3 can provide us with an excellent opportunity to observe tungsten line emissions in various kinds of charge states as a function of discharge time.



**Figure 3.** Temporal evolutions of radial profiles of electron temperature,  $T_e$ , and electron density,  $n_e$ , (a,b) for 4.0–4.8 s, (c,d) for 5.0–5.8 s, and (e,f) for 6.0–6.8 s plotted against effective minor radius,  $r_{eff}$ , normalized by  $a_{99}$ . Locations of  $r_{eff}/a_{99} = \pm 1$  are plasma edges.

### 3. Tungsten Line Emissions in the Visible, VUV, and EUV Wavelength Ranges

The results of the spectroscopic observations are summarized in this section. The identifications of charge states and the transitions are taken from the NIST database [30]. Figure 4 shows visible spectra including  $W^0$ ,  $W^{26+}$ , and  $W^{27+}$  line emissions in the wavelength range of 3200–3550 Å measured using the MK300 spectrometer.  $T_{e0}$  is also indicated for each timing of the data acquisition.  $W^{26+}$  3337.05 Å ( $4d^{10}4f^2\ ^3F, J = 4 \rightarrow 4d^{10}4f^2\ ^3F, J = 3$ ),  $W^{26+}$  3357.61 Å ( $4d^{10}4f^2\ ^3F, J = 4 \rightarrow 4d^{10}4f^2\ ^1G, J = 4$ ), and  $W^{27+}$  3377.42 Å ( $4d^{10}4f\ ^2F^\circ, J = 7/2 \rightarrow 4d^{10}4f\ ^2F^\circ, J = 5/2$ ) were observed in the spectra with  $T_{e0} = 3.0$  keV and 1.7 keV, as shown in Figure 4a,b, respectively. These  $W^{26+}$  and  $W^{27+}$  lines have already been identified as the M1 forbidden transition lines [16,17]. These lines became less significant in the spectrum with  $T_{e0} = 0.6$  keV as shown in Figure 4c, and completely disappeared in the spectrum with  $T_{e0} = 0$  keV as shown in Figure 4d. On the other hand, Figure 4d indicated that several  $W^0$  lines appeared at the wavelengths of 3205.54 Å, 3229.26 Å, 3346.19 Å, 3427.03 Å, and 3461.26 Å in the spectrum with  $T_{e0} = 0$  keV [30].

Figure 5 shows VUV spectra, including  $W^{5+}$ ,  $W^{37+}$ , and  $W^{38+}$  line emissions in the wavelength range of 250–1050 Å, measured using the VUV 109L spectrometer with  $T_{e0}$  for each timing of the data acquisition.  $W^{37+}$  646.3 Å ( $4p^64d\ ^2D, J = 5/2 \rightarrow 4p^64d\ ^2D, J = 3/2$ ),  $W^{38+}$  532.2 Å ( $4p^54d\ (3/2, 5/2)^\circ, J = 3 \rightarrow 4p^54d\ (3/2, 3/2)^\circ, J = 3$ ), and  $W^{38+}$  559.3 Å ( $4p^54d\ (3/2, 5/2)^\circ, J = 3 \rightarrow 4p^54d\ (3/2, 3/2)^\circ, J = 2$ ) were observed in the spectrum with  $T_{e0} = 3.0$  keV as shown in Figure 5a [19]. These  $W^{37+}$  and  $W^{38+}$  lines have been already identified as the M1 forbidden transition lines. These lines completely disappeared in the spectrum with  $T_{e0} = 1.7$  keV, as shown in Figure 5b. In the spectrum with  $T_{e0} = 0.6$  keV, a UTA-like broad peak was observed around 300 Å, as shown in Figure 5c. Identification of the charge states and the transitions of this UTA will be a subject of future studies. In the spectrum with  $T_{e0} = 0$  keV, two clear peaks of  $W^{5+}$  emission with  $6p \rightarrow 5d$  transition were observed at 639.62 Å and 677.34 Å, as shown in Figure 5d [18,26,30].

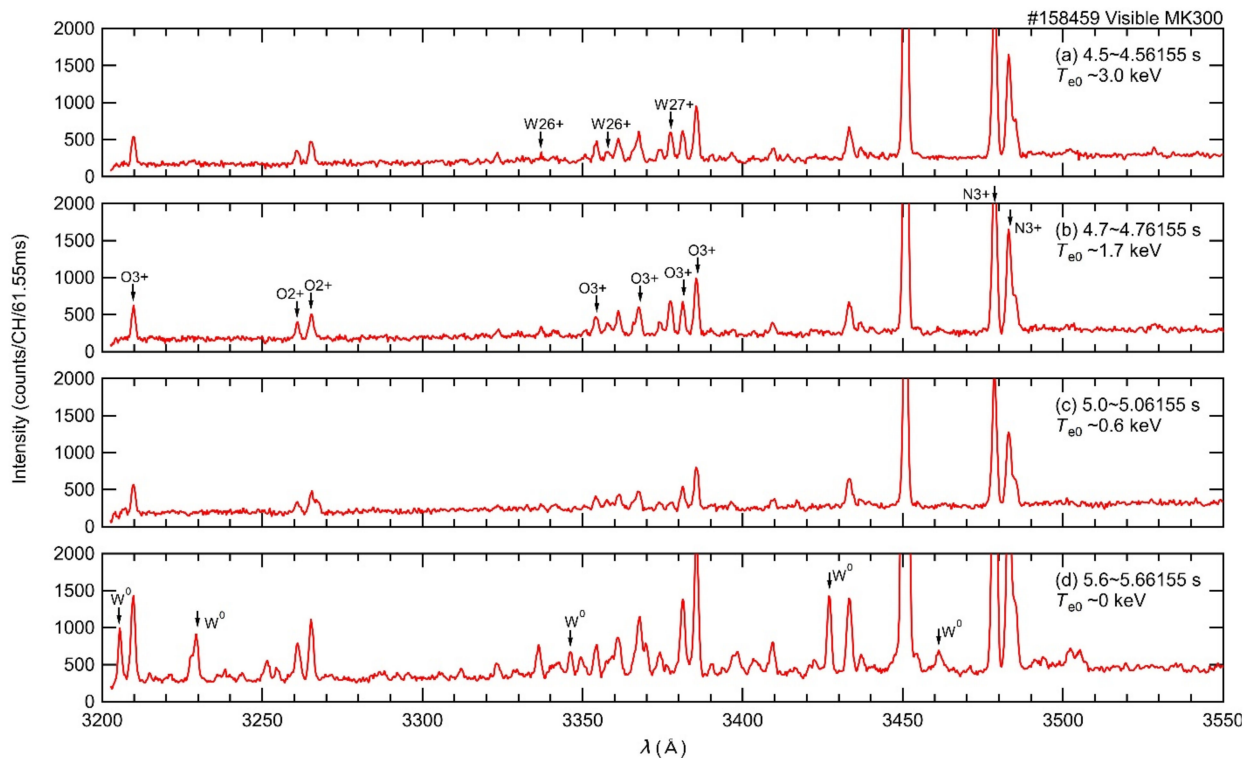


**Figure 4.** Visible spectra including  $W^0$ ,  $W^{26+}$ , and  $W^{27+}$  line emissions in the wavelength range of 3200–3550 Å measured using “MK300” spectrometer. Central electron temperature,  $T_{e0}$ , is also indicated for each timing of data acquisition. (a) 4.5–4.56155 s,  $T_{e0} \sim 3.0$  keV, (b) 4.7–4.76155 s,  $T_{e0} \sim 1.7$  keV, (c) 5.0–5.06155 s,  $T_{e0} \sim 0.6$  keV, (d) 5.6–5.66155 s,  $T_{e0} \sim 0$  keV.

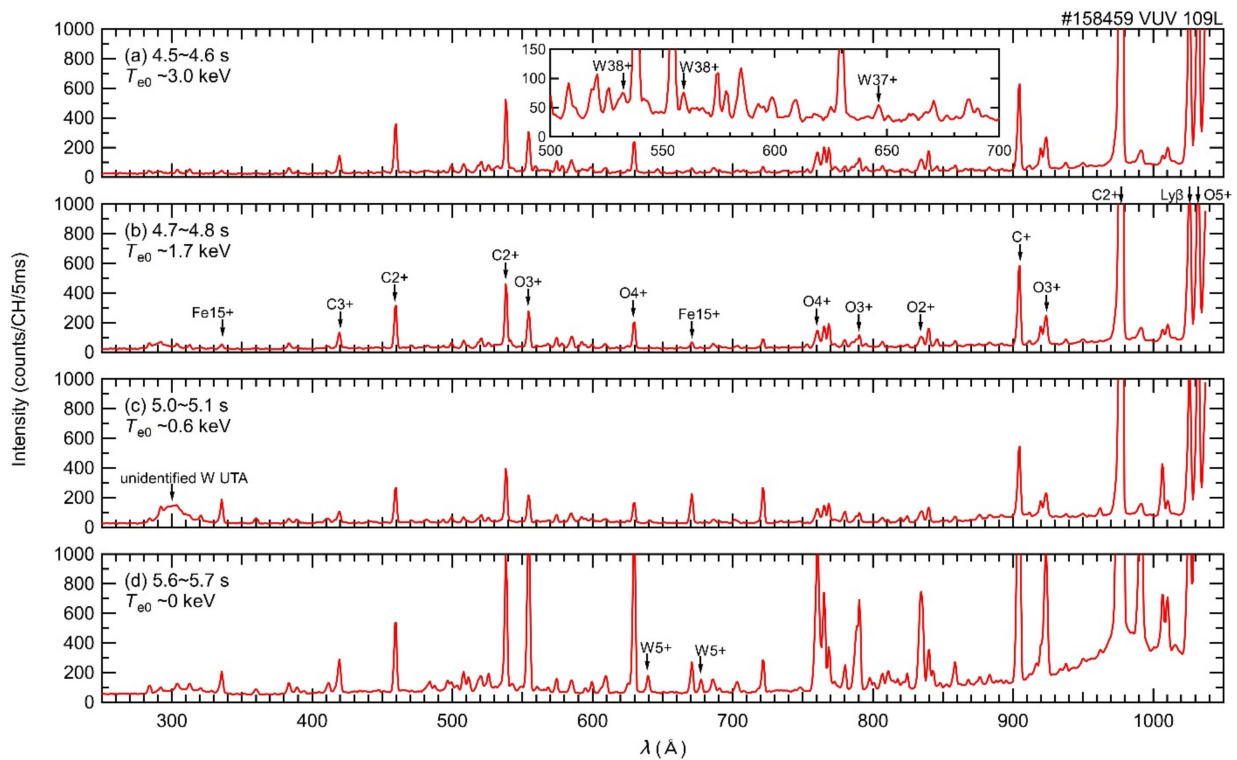


**Figure 5.** VUV spectra including  $W^{5+}$ ,  $W^{37+}$ , and  $W^{38+}$  line emissions in the wavelength range of 250–1050 Å measured using “VUV 109L” spectrometer with  $T_{e0}$  for each timing of data acquisition. (a) 4.5–4.6 s,  $T_{e0} \sim 3.0$  keV, (b) 4.7–4.8 s,  $T_{e0} \sim 1.7$  keV, (c) 5.0–5.1 s,  $T_{e0} \sim 0.6$  keV, (d) 5.6–5.7 s,  $T_{e0} \sim 0$  keV.

Figure 6 shows EUV spectra, including  $W^{6+}$ ,  $W^{7+}$ , and  $W^{41+}$ – $W^{45+}$  line emissions in the wavelength range of 100–300 Å, measured using the EUV Long spectrometer with  $T_{e0}$  for each timing of the data acquisition.  $W^{41+}$  131.15 Å ( $3d^{10}4s^24p^3^2D^{\circ}, J = 5/2 \rightarrow 3d^{10}4s^24p^3^2D^{\circ}, J = 3/2$ ),  $W^{42+}$  129.31 Å ( $3d^{10}4s^24p^2^1D, J = 2 \rightarrow 3d^{10}4s^24p^2^3P, J = 0$ ),  $W^{43+}$  126.25 Å ( $3d^{10}4s^24p^2P^{\circ}, J = 3/2 \rightarrow 3d^{10}4s^24p^2P^{\circ}, J = 1/2$ ),  $W^{44+}$  121.84 Å as the second order of  $W^{44+}$  60.93 Å ( $3d^{10}4s4p(1/2,3/2)^{\circ}, J = 1 \rightarrow 3d^{10}4s^2^1S, J = 0$ ), and  $W^{45+}$  127.06 Å ( $3d^{10}4p^2P^{\circ}, J = 1/2 \rightarrow 3d^{10}4s^2^2S, J = 1/2$ ) were observed in the spectrum with  $T_{e0} = 3.0$  keV, as shown in Figure 6a [20,30]. The  $W^{41+}$  and  $W^{43+}$  lines are M1 forbidden transition lines and the  $W^{42+}$  line is an electric-quadrupole (E2) transition. These  $W^{41+}$ – $W^{45+}$  lines completely disappeared in the spectrum with  $T_{e0} = 1.7$  keV, as shown in Figure 6b. In the spectrum with  $T_{e0} = 0.6$  keV, a broad UTA was observed around 170–200 Å, as shown in Figure 6c. It has already been reported that this UTA is primarily formed by  $n = 5 \rightarrow 5$  transitions of  $W^{7+}$ – $W^{27+}$  ions [31]. In the spectrum with  $T_{e0} = 0$  keV, two clear peaks of  $W^{6+}$  emission with  $5d \rightarrow 5p$  transition were observed at 216.17 Å and 261.31 Å, as shown in Figure 6d. These lines are recognized as useful tools to evaluate tungsten influx in tokamak experiments [32]. Moreover, several small peaks were found at around 198–202 Å in Figure 6d. They are probably  $W^{7+}$  lines because the spectral shape is similar to that of the  $W^{7+}$  spectrum identified in EBIT experiments [33,34]. The emission of  $W^{7+}$  ions in this wavelength region has been identified in detail through vacuum spark experiments with high-resolution spectroscopic diagnostics [35,36]. The spectral identification of  $W^{7+}$  ions in LHD will be improved by comparing the observed peaks with these previous studies.

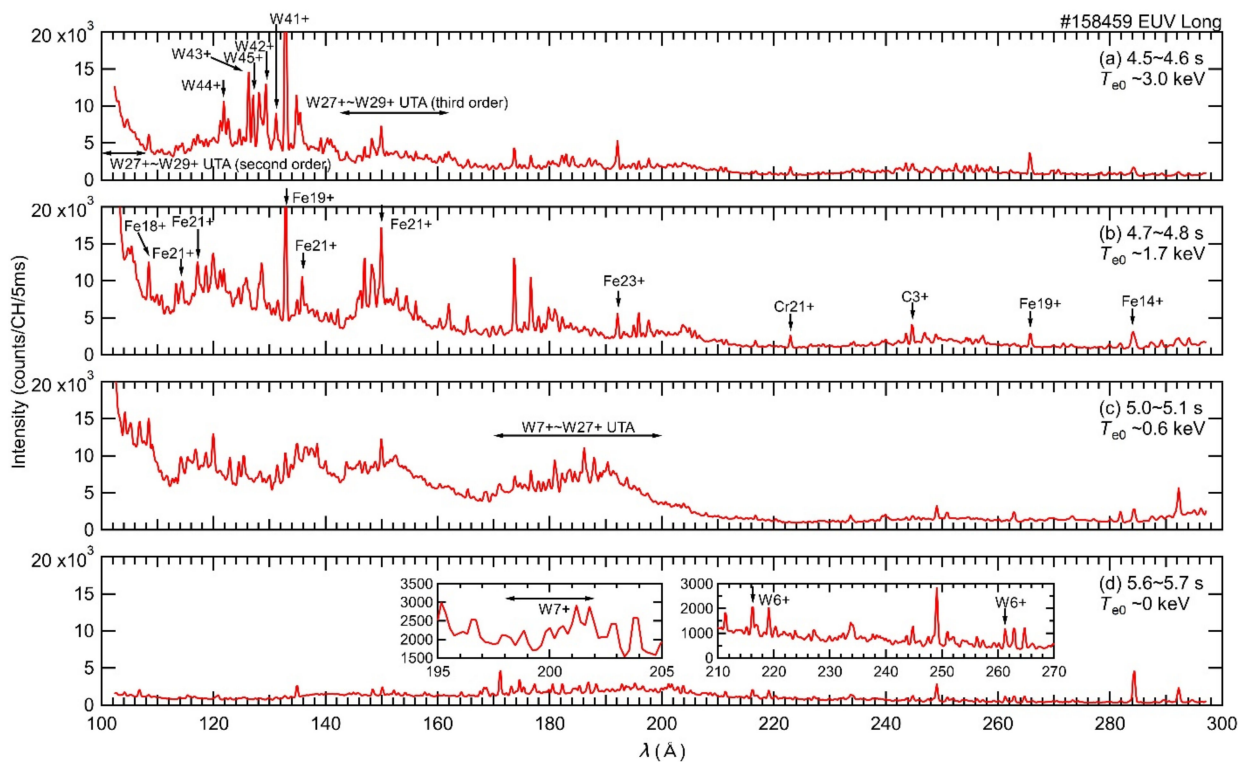


**Figure 6.** EUV spectra including  $W^{6+}$ ,  $W^{7+}$ , and  $W^{41+}$ – $W^{45+}$  line emissions in the wavelength range of 100–300 Å measured using “EUV Long” spectrometer with  $T_{e0}$  for each timing of data acquisition. (a) 4.5–4.6 s,  $T_{e0}$ ~3.0 keV, (b) 4.7–4.8 s,  $T_{e0}$ ~1.7 keV, (c) 5.0–5.1 s,  $T_{e0}$ ~0.6 keV, (d) 5.6–5.7 s,  $T_{e0}$ ~0 keV.

Figure 7 shows the EUV spectra, including  $W^{24+}$ – $W^{42+}$  UTA and  $W^{46+}$  line emissions in the wavelength range of 5–60 Å, measured using the EUV Short spectrometer with  $T_{e0}$  for each timing of the data acquisition. A  $W^{46+}$  emission line was observed at 7.93 Å as the highest charge state of tungsten ions in LHD in the spectrum with  $T_{e0} = 3.0$  keV, as shown in Figure 7a [22]. This line is a blend of an E2 transition of  $W^{46+}$  at 7.928 Å ( $3d^94s(5/2,$

1/2),  $J = 2 \rightarrow 3d^{10}1S, J = 0$ ) and a magnetic-octupole (M3) transition of  $W^{46+}$  at 7.938 Å ( $3d^94s(5/2, 1/2), J = 3 \rightarrow 3d^{10}1S, J = 0$ ). UTAs consisting of  $W^{24+}$ – $W^{33+}$  and  $W^{27+}$ – $W^{42+}$  also appeared at 19–33 Å and 46–53 Å, respectively. The identification of charge states of the UTA was performed by comparing the spectra obtained in LHD and the compact electron beam ion trap (CoBIT) with CR model calculations [11,37–39]. It is worth noting that the UTAs at around 50 Å have been used to evaluate tungsten ion concentrations in tokamak experiments [40]. More detailed discussion on determination of the tungsten ion density in LHD has also been provided using  $W^{24+}$ ,  $W^{25+}$ , and  $W^{26+}$  peaks in the UTA [41]. The spectral shape of the UTAs depended on  $T_{e0}$  in such a way that the spectral structure of  $W^{37+}$ – $W^{42+}$  at 46–48 Å disappeared in the spectrum with  $T_{e0} = 1.7$  keV as shown in Figure 7b, and  $W^{24+}$  at 32.5 Å became prominent in the spectrum with  $T_{e0} = 0.6$  keV as shown in Figure 7c. Finally, no emission lines of W ions can be seen in the spectrum with  $T_{e0} = 0$  keV as shown in Figure 7d.

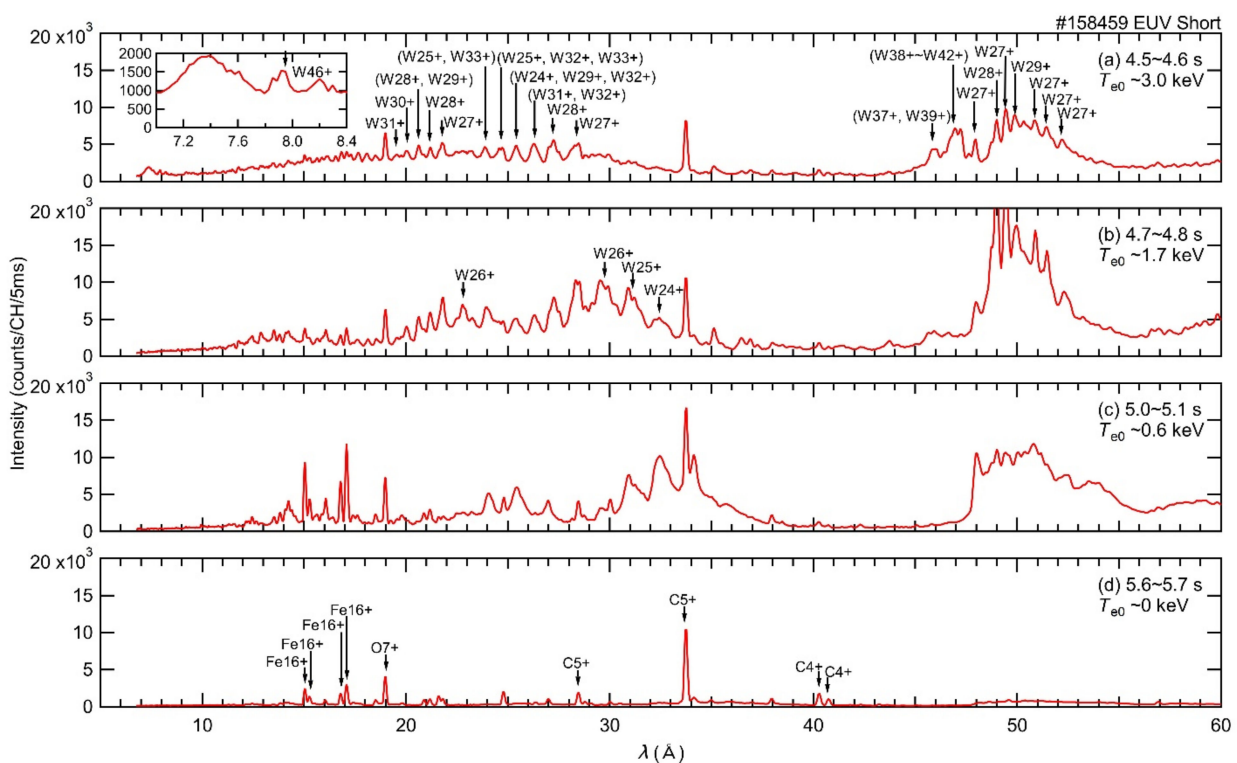


**Figure 7.** EUV spectra including  $W^{24+}$ – $W^{42+}$  UTA and  $W^{46+}$  line emissions in the wavelength range of 5–60 Å measured using “EUV Short” spectrometer with  $T_{e0}$  for each timing of data acquisition. (a) 4.5–4.6 s,  $T_{e0}$ ~3.0 keV, (b) 4.7–4.8 s,  $T_{e0}$ ~1.7 keV, (c) 5.0–5.1 s,  $T_{e0}$ ~0.6 keV, (d) 5.6–5.7 s,  $T_{e0}$ ~0 keV.

It is worthwhile to summarize the wavelengths of the emission lines observed in this study for useful tools in future spectroscopic studies. The wavelengths of  $W^0$ ,  $W^{5+}$ ,  $W^{6+}$ ,  $W^{24+}$ – $W^{28+}$ ,  $W^{37+}$ ,  $W^{38+}$ , and  $W^{41+}$ – $W^{46+}$  line emissions observed in this study are summarized in Table 1. The first and the second columns give the charge states and the ionization energies, IEs, respectively. The third and the fourth columns give the wavelengths of line emissions from the NIST database,  $\lambda_{NIST}$ , and the present observation,  $\lambda_{obs}$ , respectively. A discrepancy between  $\lambda_{NIST}$  and  $\lambda_{obs}$  is shown in the fifth column. The lower- and upper-level configurations from the NIST database are given in the sixth and the seventh columns, respectively. The eighth column gives remarks on the blended lines, the unresolved transition arrays (UTAs), or the transition types for forbidden lines. References for the line identifications or the previous observations are given in the ninth column. If no adequate item is registered in the NIST database, “-” is indicated.

**Table 1.** Wavelength list of  $W^0$ ,  $W^{5+}$ ,  $W^{6+}$ ,  $W^{24+}$ – $W^{28+}$ ,  $W^{37+}$ ,  $W^{38+}$ , and  $W^{41+}$ – $W^{46+}$  line emissions observed in this study.

$W^{q+}$	IE (eV)	$\lambda_{\text{NIST}}$ (Å)	$\lambda_{\text{obs}}$ (Å)	$\lambda_{\text{NIST}} - \lambda_{\text{obs}}$ (Å)	Lower-Level Configuration, Term, $J$	Upper-Level Configuration, Term, $J$	Remarks	References
$W^0$	7.9	3205.50	$3205.54 \pm 0.06$	−0.04	$5d^46s^2$ , $^3D, 1$	-		[30]
$W^0$	7.9	3229.23	$3229.26 \pm 0.07$	−0.03	$5d^5(^4D)6s$ , $^5D, 2$	-		[30]
$W^0$	7.9	3346.11	$3346.19 \pm 0.06$	−0.08	$5d^5(^6D)6s$ , $^7S, 3$	$5d^46s(^6D)6p$ , $^5D^{\circ}, 4$		[30]
$W^0$	7.9	3426.88 3427.72	$3427.03 \pm 0.06$	-	$5d^46s^2$ , $^3D, 1$ $5d^46s^2$ , $^3G, 3$	-	blended	[30]
$W^0$	7.9	3461.36	$3461.26 \pm 0.06$	0.1	$5d^5(^4G)6s$ , $^5G, 4$	-		[30]
$W^{5+}$	64.8	639.68	$639.62 \pm 0.09$	0.06	$5s^25p^65d$ , $^2D, 5/2$	$5s^25p^66p$ , $^2P^{\circ}, 3/2$		[18,26,30]
$W^{5+}$	64.8	677.72	$677.34 \pm 0.08$	0.38	$5s^25p^65d$ , $^2D, 3/2$	$5s^25p^66p$ , $^2P^{\circ}, 1/2$		[18,26,30]
$W^{6+}$	122.0	216.22	$216.17 \pm 0.06$	0.05	$5s^25p^6$ , $^1S, 0$	$5s^25p^5(^2P^{\circ}_{1/2})5d$ , $(1/2,3/2)^{\circ}, 1$		[30,32]
$W^{6+}$	122.0	261.39	$261.31 \pm 0.06$	0.08	$5s^25p^6$ , $^1S, 0$	$5s^25p^5(^2P^{\circ}_{3/2})5d$ , $(3/2,5/2)^{\circ}, 1$		[30,32]
$W^{24+}$	734.1	-	~27.3	-	-	-	UTA	[11,21,37–39,41]
$W^{25+}$	784.1	-	~28.4	-	-	-	UTA	[11,21,37–39,41]
$W^{26+}$	833.4	-	~29.7	-	-	-	UTA	[11,21,37–39,41]
$W^{26+}$	833.4	-	$3337.05 \pm 0.09$	-	$4d^{10}4f^2$ , $^3F, 3$	$4d^{10}4f^2$ , $^3F, 4$	M1	[16,17]
$W^{26+}$	833.4	-	$3357.61 \pm 0.08$	-	$4d^{10}4f^2$ , $^1G, 4$	$4d^{10}4f^2$ , $^3F, 4$	M1	[16,17]

Table 1. Cont.

$W^{q+}$	IE (eV)	$\lambda_{\text{NIST}}$ (Å)	$\lambda_{\text{obs}}$ (Å)	$\lambda_{\text{NIST}} - \lambda_{\text{obs}}$ (Å)	Lower-Level Configuration, Term, $J$	Upper-Level Configuration, Term, $J$	Remarks	References
$W^{27+}$	881.4	-	~31.0	-	-	-	UTA	[11,21,37–39]
$W^{27+}$	881.4	-	$3377.42 \pm 0.06$	-	$4d^{10}4f,$ $^2F^\circ, 5/2$	$4d^{10}4f,$ $^2F^\circ, 7/2$	M1	[16,17]
$W^{28+}$	1132.2	-	~32.5	-	-	-	UTA	[11,21,37–39]
$W^{37+}$	1621.7	646.7	$646.3 \pm 0.1$	0.4	$4p^64d,$ $^2D, 3/2$	$4p^64d,$ $^2D, 5/2$	M1	[19,30]
$W^{38+}$	1829.8	532.9	$532.2 \pm 0.2$	0.7	$4p^5(^2P^\circ_{3/2})4d,$ $(3/2, 3/2)^\circ, 3$	$4p^5(^2P^\circ_{3/2})4d,$ $(3/2, 5/2)^\circ, 3$	M1	[19,30]
$W^{38+}$	1829.8	559.1	$559.3 \pm 0.1$	-0.2	$4p^5(^2P^\circ_{3/2})4d,$ $(3/2, 3/2)^\circ, 2$	$4p^5(^2P^\circ_{3/2})4d,$ $(3/2, 5/2)^\circ, 3$	M1	[19,30]
$W^{41+}$	1994.8	131.22	$131.15 \pm 0.06$	0.07	$3d^{10}4s^24p^3,$ $^2D^\circ, 3/2$	$3d^{10}4s^24p^3,$ $^2D^\circ, 5/2$	M1	[20,30]
$W^{42+}$	2149.1	129.41	$129.31 \pm 0.06$	0.10	$3d^{10}4s^24p^2,$ $^3P, 0$	$3d^{10}4s^24p^2,$ $^1D, 2$	E2	[20,30]
$W^{43+}$	2210.0	126.29	$126.25 \pm 0.06$	0.04	$3d^{10}4s^24p,$ $^2P^\circ, 1/2$	$3d^{10}4s^24p,$ $^2P^\circ, 3/2$	M1	[20,30]
$W^{44+}$	2354.5	$60.93 \times 2$	$121.84 \pm 0.06$	0.02	$3d^{10}4s^2,$ $^1S, 0$	$3d^{10}4s4p,$ $(1/2,3/2)^\circ, 1$	second order	[11,20,30]
$W^{45+}$	2414.1	127.00	$127.06 \pm 0.06$	-0.06	$3d^{10}4s,$ $^2S, 1/2$	$3d^{10}4p,$ $^2P^\circ, 1/2$		[20,30]
$W^{46+}$	4057	7.928 7.938	$7.93 \pm 0.02$	-	$3d^{10},$ $^1S, 0$ $3d^{10},$ $^1S, 0$	$3d^94s,$ $(5/2,1/2), 2$ $3d^94s,$ $(5/2,1/2), 3$	E2 + M3 blended	[22,30]

As an example of an application of the summarized wavelengths, the temporal variation of emission of each charge state during the discharge is demonstrated. Figure 8 shows the temporal evolution of: Figure 8a, the heating power of ECH, n-NBI, and p-NBI, Figure 8b, the central electron temperature and line-averaged electron density,  $W^0$ – $W^{46+}$  intensities integrated over the wavelength ranges of Figure 8c, 3426.2–3427.9 Å for  $W^0$ , Figure 8d 637.8–641.2 Å for  $W^{5+}$ , Figure 8e 261.0–261.5 Å for  $W^{6+}$ , Figure 8f 32.15–32.30 Å for  $W^{24+}$ , 30.73–31.69 Å for  $W^{25+}$ , 29.29–30.40 Å for  $W^{26+}$ , Figure 8g 28.58–28.69 Å for  $W^{27+}$ , 27.35–27.78 Å for  $W^{28+}$ , Figure 8h 645.3–647.1 Å for  $W^{37+}$ , 558.6–560.3 Å for  $W^{38+}$ , Figure 8i 131.0–131.3 Å for  $W^{41+}$ , 129.2–129.5 Å for  $W^{42+}$ , 126.1–126.5 Å for  $W^{43+}$ , 126.9–127.3 Å for  $W^{45+}$ , and Figure 8j 7.89–7.95 Å for  $W^{46+}$ . The vertical axes in Figure 8c–j show the number of counts detected by the CCD, and the corresponding spectrometer is indicated by subscripts such as “ $I_{MK300}$ ”, “ $I_{VUV 109L}$ ”, “ $I_{EUV Long}$ ”, and “ $I_{EUV Short}$ ”. The signal levels in neighboring wavelength ranges with no significant line emissions were subtracted from the tungsten line intensities as background levels mainly consisting of bremsstrahlung emissions.

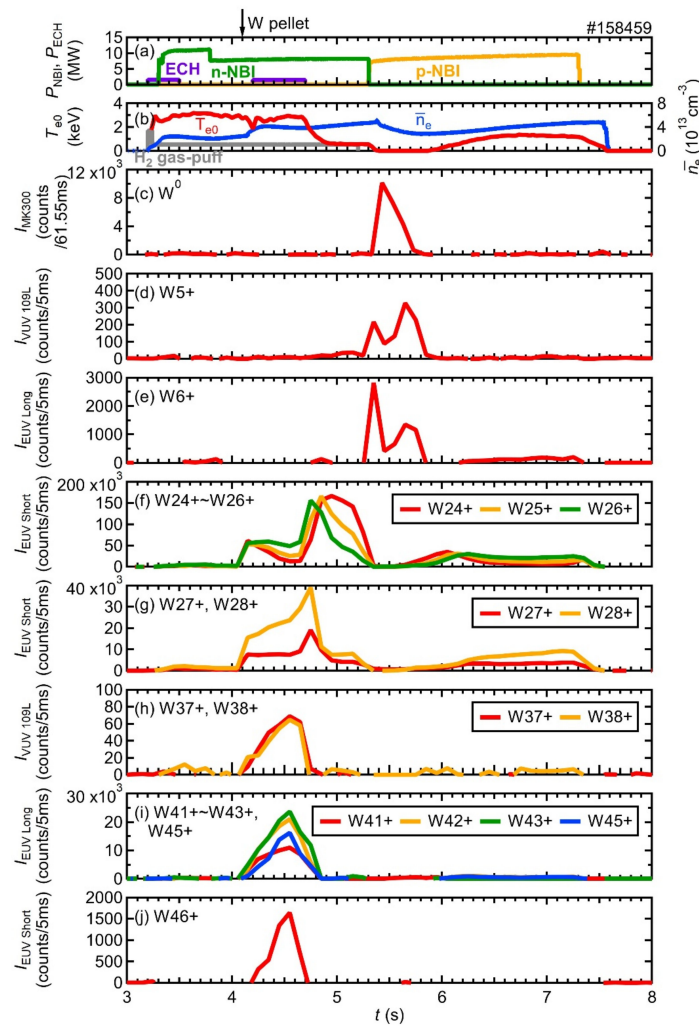


**Figure 8.** Temporal evolution of (a) heating power of ECH, n-NBI, and p-NBI, (b) central electron temperature and line-averaged electron density, and  $W^0$ – $W^{46+}$  intensities integrated over wavelength ranges of (c) 3426.2–3427.9 Å for  $W^0$ , (d) 637.8–641.2 Å for  $W^{5+}$ , (e) 261.0–261.5 Å for  $W^{6+}$ , (f) 32.15–32.30 Å for  $W^{24+}$ , 30.73–31.69 Å for  $W^{25+}$ , 29.29–30.40 Å for  $W^{26+}$ , (g) 28.58–28.69 Å for  $W^{27+}$ , 27.35–27.78 Å for  $W^{28+}$ , (h) 645.3–647.1 Å for  $W^{37+}$ , 558.6–560.3 Å for  $W^{38+}$ , (i) 131.0–131.3 Å for  $W^{41+}$ , 129.2–129.5 Å for  $W^{42+}$ , 126.1–126.5 Å for  $W^{43+}$ , 126.9–127.3 Å for  $W^{45+}$ , and (j) 7.89–7.95 Å for  $W^{46+}$ .

As shown in the figure, the emissions from medium charge states of  $W^{24+}$ – $W^{28+}$  first appeared just after the pellet injection at 4.1 s. As  $T_{e0}$  increased from 2 to 3 keV by the superposition of ECH from 4.2 to 4.7 s,  $W^{24+}$ – $W^{26+}$  decreased while  $W^{37+}$ ,  $W^{38+}$ , and  $W^{41+}$ – $W^{46+}$  increased. After the termination of ECH superposition at 4.7 s,  $W^{37+}$ ,  $W^{38+}$ , and  $W^{41+}$ – $W^{46+}$  suddenly disappeared, while  $W^{24+}$ – $W^{28+}$  recovered for some time and then began to decrease as  $T_{e0}$  decreased from 3.0 to 0.6 keV. When the NBI heating was switched from n-NBIs to p-NBIs at 5.3 s and  $T_{e0}$  approached 0 keV,  $W^{5+}$  and  $W^{6+}$  appeared first, then  $W^0$  became dominant; subsequently  $W^0$  decreased and  $W^{5+}$  and  $W^{6+}$  increased. Since the heating by the p-NBIs continued until the end of the discharge,  $W^{5+}$  and  $W^{6+}$  disappeared and  $W^{24+}$ – $W^{28+}$  appeared sequentially as  $T_{e0}$  recovered up to 1.4 keV. It has been clearly demonstrated that the dominant charge state varied sequentially, together with  $T_{e0}$ , which is a reasonable relationship between the electron temperature and the ionization energy. This is progress toward comprehensive understanding of the behavior of tungsten impurities in plasmas, but on the other hand, spectroscopic data from  $W^{10+}$  to  $W^{20+}$  are extremely insufficient. It is our future task to measure these charge regions for further understanding.

#### 4. Summary

Spectroscopic studies of emissions released from tungsten ions have been conducted in LHD for contribution to the tungsten transport study in tungsten divertor fusion devices and for expansion of the experimental database of tungsten line emissions. Tungsten ions have been distributed in the LHD plasma by injecting a pellet consisting of a small piece of tungsten metal wire enclosed by a carbon tube. Wavelengths of  $W^0$ ,  $W^{5+}$ ,  $W^{6+}$ ,  $W^{24+}$ – $W^{28+}$ ,  $W^{37+}$ ,  $W^{38+}$ , and  $W^{41+}$ – $W^{46+}$  line emissions observed in the visible, VUV, and EUV wavelength ranges have been summarized. The temporal evolution of line emissions from these charge states has been compared for comprehensive understanding of tungsten impurity behavior in a single discharge. The charge distribution of tungsten ions strongly depends on electron temperature. Measurements of emissions from  $W^{10+}$  to  $W^{20+}$  are still insufficient, which is a subject for future research.

**Author Contributions:** Conceptualization, T.O. and S.M.; methodology, T.O. and S.M.; software, T.O.; validation, T.O.; formal analysis, T.O.; investigation, T.O., S.M., D.K., I.M., H.A.S., Y.K., T.K. and M.G.; resources, T.O., Y.K., T.K. and M.G.; data curation, T.O., Y.K., T.K. and M.G.; writing—original draft preparation, T.O.; writing—review and editing, S.M., I.M. and M.G.; visualization, T.O.; supervision, S.M. and I.M.; project administration, S.M. and I.M.; funding acquisition, T.O., Y.K. and M.G. All authors have read and agreed to the published version of the manuscript.

**Funding:** This work was partially supported by JSPS KAKENHI grant numbers 17K14426 and 20K03896.

**Data Availability Statement:** Data are available on request.

**Acknowledgments:** The authors thank all the members of the LHD team for their cooperation with the LHD operation.

**Conflicts of Interest:** The authors declare no conflict of interest.

#### References

1. ITER Physics Basis Editors; ITER Physics Expert Group Chairs and Co-Chairs; ITER Joint Central Team and Physics Integration Unit. Chapter 1: Overview and summary. *Nucl. Fusion* **1999**, *39*, 2137–2174. [[CrossRef](#)]
2. Neu, R.; Dux, R.; Kallenbach, A.; Pütterich, T.; Balden, M.; Fuchs, J.C.; Herrmann, A.; Maggi, C.F.; O’Mullane, M.; Pugno, R.; et al. Tungsten: An option for divertor and main chamber plasma facing components in future fusion devices. *Nucl. Fusion* **2005**, *45*, 209–218. [[CrossRef](#)]
3. Roth, J.; Tsitrone, E.; Loarer, T.; Philipps, V.; Brezinsek, S.; Loarte, A.; Counsell, G.F.; Doerner, R.P.; Schmid, K.; Ogorodnikova, O.V.; et al. Tritium inventory in ITER plasma-facing materials and tritium removal procedures. *Plasma Phys. Control. Fusion* **2008**, *50*, 103001. [[CrossRef](#)]
4. Kramida, A.E.; Shirai, T. Energy levels and spectral lines of tungsten, W III through W LXXIV. *At. Data Nucl. Data Tables* **2009**, *95*, 305–474. [[CrossRef](#)]

5. Clementson, J.; Beiersdorfer, P. Wavelength measurement of  $n = 3$  to  $n = 3$  transitions in highly charged tungsten ions. *Phys. Rev. A* **2010**, *81*, 52509. [CrossRef]
6. Podpaly, Y.; Clementson, J.; Beiersdorfer, P.; Williamson, J.; Brown, G.V.; Gu, M.F. Spectroscopy of  $2s_{1/2} - 2p_{3/2}$  transitions in  $W^{65+}$  through  $W^{71+}$ . *Phys. Rev. A* **2009**, *80*, 52504. [CrossRef]
7. Ralchenko, Y.; Reader, J.; Pomeroy, J.M.; Tan, J.N.; Gillaspay, J.D. Spectra of  $W^{39+} - W^{47+}$  in the 12–20 nm region observed with an EBIT light source. *J. Phys. B At. Mol. Opt. Phys.* **2007**, *40*, 3861–3875. [CrossRef]
8. Yanagibayashi, J.; Nakano, T.; Iwamae, A.; Kubo, H.; Hasuo, M.; Itami, K. Highly charged tungsten spectra observed from JT-60U plasmas at  $T_e \approx 8$  and 14 keV. *J. Phys. B At. Mol. Opt. Phys.* **2010**, *43*, 144013. [CrossRef]
9. Pütterich, T.; Neu, R.; Dux, R.; Whiteford, A.D.; O'Mullane, M.G.; the ASDEX Upgrade Team. Modelling of measured tungsten spectra from ASDEX Upgrade and predictions for ITER. *Plasma Phys. Control. Fusion* **2008**, *50*, 85016. [CrossRef]
10. Pütterich, T.; Neu, R.; Biedermann, C.; Radtke, R.; ASDEX Upgrade Team. Disentangling the emissions of highly ionized tungsten in the range 4–14 nm. *J. Phys. B At. Mol. Opt. Phys.* **2005**, *38*, 3071–3082. [CrossRef]
11. Morita, S.; Dong, C.F.; Goto, M.; Kato, D.; Murakami, I.; Sakaue, H.A.; Hasuo, M.; Koike, F.; Nakamura, N.; Oishi, T.; et al. A Study of tungsten spectra using Large Helical Device and Compact Electron Beam Ion Trap in NIFS. *AIP Conf. Proc.* **2013**, *1545*, 143–152. [CrossRef]
12. Morita, S.; Dong, C.F.; Kato, D.; Liu, Y.; Zhang, L.; Cui, Z.Y.; Goto, M.; Kawamoto, Y.; Murakami, I.; Oishi, T. Quantitative analysis on tungsten spectra of  $W^{6+}$  to  $W^{45+}$  ions. *J. Phys. Conf. Ser.* **2019**, *1289*, 12005. [CrossRef]
13. Huang, X.L.; Morita, S.; Oishi, T.; Goto, M.; Zhang, H.M. Coaxial pellets for metallic impurity injection on the large helical device. *Rev. Sci. Instrum.* **2014**, *85*, E811–E818. [CrossRef] [PubMed]
14. Oishi, T.; Morita, S.; Huang, X.L.; Liu, Y.; Goto, M.; The LHD Experiment Group. Response of plasmas to tungsten pellet injection in neutral beam heated discharges in Large Helical Device. *Plasma Fusion Res.* **2018**, *13*, 3402031. [CrossRef]
15. Kato, D.; Goto, M.; Morita, S.; Murakami, I.; Sakaue, H.A.; Ding, X.B.; Sudo, S.; Suzuki, C.; Tamura, N.; Nakamura, N.; et al. Observation of visible forbidden lines from highly charged tungsten ions at the large helical device. *Phys. Scr.* **2013**, *T156*, 14081. [CrossRef]
16. Kato, D.; Sakaue, H.A.; Murakami, I.; Goto, M.; Oishi, T.; Fujii, K.; Nakamura, N.; Morita, S.; LHD Experiment Group. Observation of Visible Forbidden Lines of Tungsten Highly Charged Ions in LHD Core Plasmas and Its Application to Ion Distribution Analysis. Preprint: 26th IAEA Fusion Energy Conf. (2016, Kyoto) EX/P8-14. Available online: <https://nucleus.iaea.org/sites/fusionportal/Shared%20Documents/FEC%202016/fec2016-preprints/preprint0240.pdf> (accessed on 1 September 2021).
17. Kato, D.; Sakaue, H.A.; Murakami, I.; Goto, M.; Oishi, T.; Tamura, N.; Funaba, H.; Morita, S. Assessment of W Density in LHD Core Plasmas Using Visible Forbidden Lines of Highly Charged W Ions. *Nucl. Fusion* **2021**, in press. [CrossRef]
18. Oishi, T.; Morita, S.; Huang, X.L.; Zhang, H.M.; Goto, M.; The LHD Experiment Group. Observation of W IV–W VII line emissions in wavelength range of 495–1475 Å in the large helical device. *Phys. Scr.* **2016**, *91*, 25602. [CrossRef]
19. Oishi, T.; Morita, S.; Kato, D.; Murakami, I.; Sakaue, H.A.; Kawamoto, Y.; Goto, M.; The LHD Experiment Group. Identification of forbidden emission lines from highly ionized tungsten ions in VUV wavelength range in LHD for ITER edge plasma diagnostics. *Nucl. Mater. Energy* **2021**, *26*, 100932. [CrossRef]
20. Liu, Y.; Morita, S.; Oishi, T.; Goto, M.; Huang, X.L. Observation of Tungsten Line Emissions in Wavelength Range of 10–500 Å in Large Helical Device. *Plasma Fusion Res.* **2018**, *13*, 3402020. [CrossRef]
21. Liu, Y.; Morita, S.; Huang, X.L.; Oishi, T.; Goto, M.; Zhang, H.M. Component investigation of ionization stages on tungsten unresolved transition array spectra for plasma diagnostics based on space-resolved extreme-ultra violet spectroscopy in large helical device. *J. Appl. Phys.* **2017**, *122*, 233301. [CrossRef]
22. Oishi, T.; Morita, S.; Kato, D.; Murakami, I.; Sakaue, H.A.; Kawamoto, Y.; Goto, M. Observation of line emissions from Ni-like  $W^{46+}$  ions in wavelength range of 7–8 Å in the Large Helical Device. *Phys. Scr.* **2021**, *96*, 25602. [CrossRef]
23. Takeiri, Y.; Morisaki, T.; Osakabe, M.; Yokoyama, M.; Sakakibara, S.; Takahashi, H.; Nakamura, Y.; Oishi, T.; Motojima, G.; Murakami, S.; et al. Extension of the operational regime of the LHD towards a deuterium experiment. *Nucl. Fusion* **2017**, *57*, 102023. [CrossRef]
24. Chowdhuri, M.B.; Morita, S.; Goto, M. Characteristics of an absolutely calibrated flat-field extreme ultraviolet spectrometer in the 10–130 Å range for fusion plasma diagnostics. *Appl. Opt.* **2008**, *47*, 135–146. [CrossRef] [PubMed]
25. Chowdhuri, M.B.; Morita, S.; Goto, M.; Nishimura, H.; Nagai, K.; Fujioka, S. Spectroscopic comparison between 1200 grooves/mm ruled and holographic gratings of a flat-field spectrometer and its absolute sensitivity calibration using bremsstrahlung continuum. *Rev. Sci. Instrum.* **2007**, *78*, 23501. [CrossRef] [PubMed]
26. Oishi, T.; Morita, S.; Huang, X.L.; Zhang, H.M.; Goto, M.; The LHD Experiment Group. Line Spectrum of Tungsten Ions at Low Ionization Stages in Large Helical Device in Wavelength Range of 300–2400 Å Measured Using 20 cm Normal Incidence VUV Spectrometers. *Plasma Fus. Res.* **2015**, *10*, 3402031. [CrossRef]
27. Zhou, H.Y.; Morita, S.; Goto, M.; Dong, C.F.  $Z_{\text{eff}}$  profile diagnostics using visible bremsstrahlung continuum for nonaxisymmetric plasmas with finite  $\beta$  in large helical device. *J. Appl. Phys.* **2010**, *107*, 53306. [CrossRef]
28. Kawamoto, Y.; Morita, S.; Goto, M.; Oishi, T. Qualitative Improvement of  $Z_{\text{eff}}$  Diagnostic Based on Visible Bremsstrahlung Profile Measurement by Changing Observation Cross Section in LHD. *Plasma Fus. Res.* **2021**, *16*, 2402072. [CrossRef]

29. Watanabe, K.Y.; Suzuki, Y.; Yamaguchi, T.; Narihara, K.; Tanaka, K.; Tokuzawa, T.; Yamada, I.; Sakakibara, S.; Narushima, Y.; Morisaki, T.; et al. Change of plasma boundaries due to beta in heliotron plasma with helical divertor configuration. *Plasma Phys. Controlled Fusion* **2007**, *49*, 605–618. [[CrossRef](#)]
30. Kramida, A.; Ralchenko, Y.; Reader, J.; NIST ASD Team. *NIST Atomic Spectra Database, (ver. 5.8)*; National Institute of Standards and Technology: Gaithersburg, MD, USA, 2020. Available online: <https://physics.nist.gov/asd> (accessed on 17 August 2021). [[CrossRef](#)]
31. Suzuki, C.; Harte, C.S.; Kilbane, D.; Kato, T.; Sakaue, H.A.; Murakami, I.; Kato, D.; Sato, K.; Tamura, N.; Sudo, S.; et al. Interpretation of spectral emission in the 20 nm region from tungsten ions observed in fusion device plasmas. *J. Phys. B At. Mol. Opt. Phys.* **2011**, *44*, 175004. [[CrossRef](#)]
32. Dong, C.F.; Morita, S.; Cui, Z.Y.; Sun, P.; Zhang, K.; Murakami, I.; Zhang, B.Y.; Yang, Z.C.; Zheng, D.L.; Feng, L.; et al. Evaluation of tungsten influx rate and study of edge tungsten behavior based on the observation of EUV line emissions from  $W^{6+}$  ions in HL-2A. *Nucl. Fusion* **2019**, *59*, 16020. [[CrossRef](#)]
33. Mita, M.; Sakaue, H.A.; Kato, D.; Murakami, I.; Nakamura, N. Direct Observation of the M1 Transition between the Ground Term Fine Structure Levels of W VIII. *Atoms* **2017**, *5*, 13. [[CrossRef](#)]
34. Clementson, J.; Lennartsson, T.; Beiersdorfer, P. Extreme ultraviolet spectra of few-times ionized tungsten for divertor plasma diagnostics. *Atoms* **2015**, *3*, 407–421. [[CrossRef](#)]
35. Ryabtsev, A.; Kononov, E.; Kildiyarova, R.; Tchang-Brillet, W.-Ü.L.; Wyart, J.F.; Champion, N.; Blaess, C. Spectra of W VIII and W IX in the EUV region. *Atoms* **2015**, *3*, 273–298. [[CrossRef](#)]
36. Ryabtsev, A.; Kononov, E.Y.; Kildiyarova, R.; Tchang-Brillet, W.-Ü.L.; Wyart, J.F. The spectrum of seven times ionized tungsten (W VIII) relevant to tokamak divertor plasmas. *Phys. Scr.* **2013**, *87*, 45303. [[CrossRef](#)]
37. Sakaue, H.A.; Kato, D.; Ding, X.B.; Murakami, I.; Koike, F. Spectroscopy of highly charged tungsten ions with Electron Beam Ion Traps. *AIP Conf. Proc.* **2012**, *1438*, 91–96. [[CrossRef](#)]
38. Murakami, I.; Sakaue, H.A.; Suzuki, C.; Kato, D.; Goto, M.; Tamura, N.; Sudo, S.; Morita, S.; LHD Experiment Group. Development of quantitative atomic modeling for tungsten transport study using LHD plasma with tungsten pellet injection. *Nucl. Fusion* **2015**, *55*, 93016. [[CrossRef](#)]
39. Murakami, I.; Kato, D.; Oishi, T.; Goto, M.; Kawamoto, Y.; Suzuki, C.; Sakaue, H.A.; Morita, S.; LHD Experiment Group. Progress of tungsten spectral modeling for ITER edge plasma diagnostics based on tungsten spectroscopy in LHD. *Nucl. Mater. Energy* **2021**, *26*, 100923. [[CrossRef](#)]
40. Zhang, L.; Morita, S.; Xu, Z.; Zhang, P.F.; Zang, Q.; Duan, Y.M.; Liu, H.Q.; Zhao, H.L.; Ding, F.; Ohishi, T.; et al. Suppression of tungsten accumulation during ELMy H-mode by lower hybrid wave heating in the EAST tokamak. *Nucl. Mater. Energy* **2017**, *12*, 774–778. [[CrossRef](#)]
41. Liu, Y.; Morita, S.; Murakami, I.; Oishi, T.; Goto, M.; Huang, X.L. Density evaluation of tungsten  $W^{24+}$ ,  $W^{25+}$ , and  $W^{26+}$  ions using unresolved transition array at 27–34 Å in Large Helical Device. *Jpn. J. Appl. Phys.* **2018**, *57*, 106101. [[CrossRef](#)]